Biomaterials Science

ROYAL SOCIETY OF CHEMISTRY

PAPER

View Article Online
View Journal | View Issue

Cite this: *Biomater. Sci.*, 2022, **10**, 3110

Adipose mesenchymal stem cell-based tissue engineering mesh with sustained bFGF release to enhance tissue repair

Xiaotong Wu,[a,b] Hong Guo,[c] Yuanyuan Jia,[a,b] Qing Wang,[a,b] Jiaqi Wang,[a,b] Xiuli Sun*[a,b] and Jianliu Wang*[a,b]

Pelvic organ prolapse (POP) harms the quality of life of elderly patients. Transvaginal polypropylene mesh repair for POP was a frequently reported complication and was banned by the FDA in 2019. New therapeutic strategies are urgently required, and tissue engineering technology could be a novel therapy. Here, we developed a tissue engineering mesh out of three components: silk fibroin (SF) knitted mesh loaded with basic fibroblast growth factor (bFGF) and adipose-derived stem cells (ADSCs). We used coaxial electrospinning technology to achieve local bFGF release to promote regeneration. Additionally, ADSCs were loaded to demonstrate their paracrine ability of immune regulation and angiogenesis. Meanwhile, knitted silk fibroin mesh provided mechanical support. *In vitro*, SF/bFGF/ADSC tissue engineering mesh can stably release bFGF and has good biocompatibility, promoting cell proliferation and extracellular matrix synthesis. Six months after the SF/bFGF/ADSC tissue engineering mesh was implanted in a SD rat model, extracellular matrix reorganization, angiogenesis, and immunomodulatory effect, as well as mechanical properties of the implanting position were improved. Hence, SF/bFGF/ADSC tissue engineering mesh could be regarded as a promising option with excellent collagen synthesis, low foreign body response, and early angiogenic ability, providing potential ideas for POP treatment.

Received 9th December 2021,
Accepted 26th March 2022

DOI: 10.1039/d1bm01893k

rsc.li/biomaterials-science

Introduction

Pelvic organ prolapse (POP) is a common disease in middle-aged and older women. Surgery is the primary method of treatment for severe POP. Data from both home and abroad revealed that the recurrence rate of autologous tissue repair was 30%–40% within five years of surgery.[1] However, the rate of secondary surgery due to specific complications such as exposure, infection and pain is significantly higher than the rate of secondary surgery due to autologous tissue repair surgery.[2] The polypropylene mesh used for SUI and POP treatment began to decline after warnings of complications in 2008 and 2011, owing to the belief of the Food and Drug Administration (FDA) that it is more dangerous. The FDA classified transvaginal mesh as a high-risk class III device in 2016. In 2018, the United Kingdom, Australia, and New Zealand banned their use entirely, and many mesh products were withdrawn.[3–5] It ordered the use of all mesh materials, including polypropylene slings, for SUI treatment to be discontinued in the UK and Ireland. In April 2019, the FDA prohibited the production of transvaginal mesh in the United States.[6] Polypropylene mesh was still being used in China, and gynaecologists attempted to replace it with autologous tissue repair or extracellular matrix products. The mechanical environment and anatomical structure of the female pelvic floor are complex. In contrast to skeletal muscle ligaments, pelvic floor ligaments are more likely to extend or thicken the peritoneum and are primarily composed of fibroblasts and extracellular matrix (ECM) components such as type I or III collagen and elastin.[7]

Using stem cells has greatly aided the development of tissue engineering. They can significantly improve the function of target organs by regulating apoptosis and inflammation and promoting proliferation.[8,9] Adult stem cells can be auto-grafted without ethical or legal issues, and they can overcome mutations and other adverse effects.[10] The commonly used adult stem cells include bone marrow mesenchymal stem cells (BMSCs), endometrial mesenchymal stem cells (EMSCs), and adipose mesenchymal stem cells (ADSCs). Because adipose tissue is abundant and relatively easy to obtain, ADSCs have the most advantages in cell therapy and tissue engineering. It has been reported that ADSCs undergo senescence later than BMSCs,[11] and have a higher proliferation capability than

[a]*Department of Obstetrics and Gynecology, Peking University People's Hospital, Beijing, China. E-mail: wangjianliu1203@163.com, sunxiuli918@126.com*
[b]*Beijing Key Laboratory of Female Pelvic Floor Disorders, Beijing, China*
[c]*Donghua University College of Textiles, Shanghai, China*

BMSCs.[12] ADSCs also have a more active paracrine capacity than other types of stem cells.[13] The microenvironment of the implantation site influences stem cell proliferation and differentiation, and the spatial structure of ECM and local growth factors are the main factors that contribute to the microenvironment's specificity.[14,15] Through mechanical and physical signals, spatial structure can control stem cell differentiation. Nanofibers can provide stem cells with a three-dimensional environment similar to that of the ECM, allowing cell adhesion, growth, differentiation, and paracrine function, ultimately achieving repair and regeneration.[16,17] The basic fibroblast growth factor (bFGF) is a key active factor in the ECM of pelvic floor tissues. BFGF has been demonstrated to significantly promote stem cell differentiation into fibroblasts and significantly increase the expression of ligament-related extracellular matrix and cytoskeletal components.[18] Hence, long-term maintenance of bFGF at an effective concentration can provide an appropriate microenvironment for stem cell differentiation.

Based on the coaxial electrospinning technology, nanofiber scaffolds are regarded as excellent and effective ECM simulation systems and biological molecule transmission systems, which can provide physical support for the cells to grow and guide the differentiation of stem cells and ultimately affect their ability to repair regeneration.[19] Its core–shell structure can load various drugs, such as growth factors in the fiber,[20] thus reducing drug dose, protecting drug activity and maintaining drug release at the site, which is widely used in tissue engineering and drug controlled release areas.[21]

Silk fibroin is a type of natural fibrin derived from silkworm cocoons that has been widely used in tissue engineering and regenerative medicine due to its excellent mechanical properties and biocompatibility.[22,23] In this study, silk fibroin nanofiber scaffolds were prepared using the coaxial electrical spinning technology for both sustained release of bFGF and simulation of extracellular matrix, providing a suitable microenvironment for stem cell differentiation and promoting pelvic floor tissue regeneration. The paracrine function of stem cells combined with bFGF was used at the beginning of tissue-engineered scaffold implantation to accelerate cell growth and extracellular matrix reconstruction while inhibiting the acute inflammatory response. Later on, stem cells differentiated into fibroblasts in response to continuous microenvironmental stimulation, speeding up pelvic floor tissue reconstruction. The combination of growth factors and nanostructures will speed up the repair of pelvic floor tissue by combining paracrine and directed differentiation, breaking through the bottleneck of insufficient regeneration and repair of pelvic floor mesh and laying the groundwork for clinical transformation.

Methods

Preparation of SF solution

The cocoon was cut to prepare an 8 mM urea solution at a 1 : 30 ratio in a 90 °C water bath heated for 3 h. Deionized water was thoroughly washed, dried, and repeated three times. After dialysis, the degummed fibre and 9.3 mM lithium bromide solution were dissolved in a 60 °C water bath at a 1 : 10 ratio and freeze-dried after dialysis for 48 h.

Preparation of sustained release bFGF three-dimensional nanofiber scaffolds (3DNS)

The core layer was a 5 μg mL^{-1} bFGF (Peprotech, 400-29) and FBS (Gibco) mixed solution, and the shell was an SF/PVA blend solution, dissolved in formic acid, stirred at room temperature for 3 h, ultrasonically cleaned for 5 min, and stood for 1 h of defoaming. The spinning solution was loaded into the needle #21 syringe after being completely defoamed, and the syringe was then installed on the propeller. The following parameters were set: a spinning solution concentration of 13%, a voltage of 19 kV, a receiving distance of 17 cm, a pushing speed of 0.7 mL h^{-1}, and a continuous spinning time of 6 h.

Mechanical properties test of 3DNS and tissue

The 3DNS breaking strength (unit: N) and breaking elongation (unit: mm) were tested using a YG (B) 026G-500 medical textile multifunctional strength instrument. The sample size were 1 × 4 cm, the interval was 20 mm and the speed was 10 mm min^{-1}, each sample was tested at least three times. The tensile properties of the tissue were tested using an AGS-X electronic universal testing machine. The sample size was 20 × 20 mm. The test conditions were adjusted following GB/T 3923.1-1997. The preadded tension is 1 N. The maximum force recorded by the specimen being pulled during the tensile test is the breaking strength (unit N), which is the absolute value of the material strength.

Physical properties of 3DNS

The sample was cut into 3 × 3 cm pieces using a PMICFP-1100AI pore size analyzer. The sample was placed into the cavity after being wet. The pore size and distribution of the sample were determined by calculating the pressure and flow changes of air passing through dry and wet samples. The infrared spectra of the RSF (regenerated silk fibroin) powder, PVA particles, RSF nanofiber scaffold, and RSF/PVA nanofiber scaffold were tested and analyzed using a NEXUS-670 Fourier infrared spectrometer.

Detection of drug release of the 3DNS

The scaffolds were cut into 1 × 1 cm pieces and placed in a 1 mL PBS buffer solution. The drug release experiment took place on a 4 °C shaking table with five wells. Then, 0.5 mL of the supernatant was taken every day and stored at −20 °C, and PBS was added.

The bFGF secretion was detected using ELISA kit instructions.

Cell viability and cell proliferation assessment

The viability of ADSCs seeded on 3DNS was determined by a live/dead kit and CCK8 cell proliferation detection. P3 ADSCs were used in the study, and both the identification and iso-

lation processes were isolated as before.[24] The cell density in the scaffold was adjusted to 10^6 cells per mL. The scaffolds were evenly coated with staining solution and cultured at 37 °C for 15 min. The living cells fluoresced green, while the dead cells fluoresced red. The scaffold was cut to approximately 0.5 × 0.5 cm in size to cover the bottom of the 96-well plate completely and cocultured with ADSCs. Ten microliters of CCK8 solution was added to each well and incubated at 37 °C for 2 h. For seven days, five wells from each group were collected for analysis.

Scanning electron microscopy

The ADSCs were cocultured with the scaffold and fixed with 2.5% glutaraldehyde. The fixative was removed, washed twice with PBS, and again fixed with 1% osmic acid for 1 h. Different concentrations of alcohol gradient dehydration, vacuum drying, conductive treatment, and microscopic observation were performed.

ADSCs differentiated into fibroblast cells

The ADSCs were divided into three groups, with a cell density of 1×10^5 mL^{-1}: the control group (cells inoculated and cultured in DMEM-F12 containing 10% FBS in TCPs), the two-dimensional (2D) group (cells inoculated and cultured in DMEM-F12 containing 10% FBS and 20 ng mL^{-1} bFGF in TCPs) and 3DNS experimental group (cells inoculated and cultured in DMEM-F12 containing 10% FBS in scaffolds). Each group received three parallel samples. The medium was changed daily. Cell survival was observed using an inverted microscope. Subsequent research was conducted. The cells were then identified by fibroblast-specific protein 1 (FSP 1) immunohistochemistry.

Immunofluorescence assay

The three groups were fixed in 4% (w/v) paraformaldehyde (Sigma) rinsing agent for 30 min and then permeabilized with 0.25% Triton X-100 (Sigma) at room temperature (RT) for 10 min and blocking solution (10% goat serum in PBS) for 30 min at room temperature. The blocking reagents were discarded, and the primary antibody was incubated overnight at 4 °C. FSP-1 (1 : 200, Abcam) and vinculin were the primary antibodies (1 : 100, CST). The cells were washed three times with a rinsing agent after incubation. Following that, the cells were incubated for 60 min at room temperature in the dark with a FITC-labelled secondary antibody. The cells were then washed with a rinsing agent, and the nuclei were stained with DAPI. Images were taken using a fluorescence microscope (Nikon, USA). The cell cytoskeleton was visualized using F-actin/DAPI staining. After rinsing with PBS, the three groups were fixed with 4% paraformaldehyde for 15 min. F-Actin was stained with 2.5% phalloidin (Invitrogen, A22287) for 30 min and with 0.1 μg mL^{-1} DAPI (Invitrogen, 62247). Images were taken using a fluorescence microscope (Nikon, USA). Five sections were randomly selected from each group for analysis, and ten fields were selected under a 400× fluorescence microscope for positive cell counts in each section. Following that, each sample's vessel was evaluated. Five sections were chosen at random from each group, and ten fields were selected under a 400× fluorescence microscope for vessel counting in each section.

Western blot analysis

To find the expression level of related proteins, three groups of total proteins were extracted from cells using a radioimmunoprecipitation assay buffer containing PMSF (Cat. No. R0010; Solarbio Biotechnology Co., Ltd, Beijing), incubated on ice for 30 min, and then centrifuged at 4 °C for 10 min (12 000*g*) to obtain the supernatant. The BCA kit (catalogue number 23225; Thermo Fisher Scientific, Inc.) was used to assess the protein concentration of each sample supernatant, and deionized water was used to adjust the amount of protein. A 10% SDS–PAGE gel was prepared (catalog number P0012A; Beyotime Institute of Biotechnology, Shanghai, China), and a 50 μg protein sample was added to each well. For 2 h, electrophoresis was carried out at a constant voltage of 80 V. The protein was transferred to a polyvinylidene fluoride (PVDF) membrane at 110 V for 2 h. PVDF membrane was then blocked with TBST buffer containing 5% skimmed milk powder for 2 h. The membrane was then washed with TBST and incubated with rabbit polyclonal ColIA1 (1 : 1000; CST), Col III A1 (1 : 1000; NOVUS), and GAPDH antibody (1 : 2000; Abcam). The grey intensity of the protein band was quantified by ImageJ and normalized to GAPDH. Integrin β1, FAK, p-FAK (Tyr397), ERK, p-ERK (Thr202/Tyr204), and FN antibodies were obtained from CST. They were kept at 4 °C overnight before being washed with TBST three times, each for 10 min. The membrane was washed three times at room temperature with 0.1% PBS/Tween-20 (PBST) for 10 min each time before being immersed in the enhanced chemiluminescence reaction solution. Expanded GAPDH was used as an internal reference grayscale target protein strip. The relative protein expression was calculated by dividing the grey values of the target protein band by the grey values of the internal reference band and was assessed at least three times.

Construction of tissue engineering meshes

Using electrostatic adsorption to different groups of nano scaffold (bFGF obtained or not) compound on the silk fibroin mesh, the meshes were cut into 1 × 1 cm size in 6-well plates, PBS soaked for 2 h, cell density adjusted to 2×10^6 mL^{-1}, the cell suspension added to the composite mesh and stood for 2 h and the medium supplemented, cultured at 37 °C, 5% CO_2, and subsequent animal experiments were carried out.

Surgically SD rat model

The laboratory animal unit of Peking University People's Hospital in Beijing, China, provided 90 female SD rats aged eight weeks (205 ± 15 g). The IRB of Peking University People's Hospital approved the use of animals and the experimental protocols (2020PHE033). The rats were raised in a standard laboratory setting with free access to food and water. Animals were housed for one week before the study to allow them to acclimate. Isoflurane was inhaled at a 5 cc min^{-1} rate and

maintained at 2 cc min^{-1}. Abdominal skin was disinfected three times, in both side white line remove the external and internal oblique, build a 1 cm × 1 cm size rat abdominal wall defect model, the tissue engineering mesh was used to repair the defect, 5–0 absorbable surgical sutures fixed the mesh edge to the surrounding tissue of the abdominal wall defect without tension. The incisions were sutured layer by layer and disinfected with 75% alcohol and executed regularly.

Histological staining

After being fixed with paraformaldehyde for 24 h, the samples were dehydrated in an alcohol gradient and sectioned on a paraffin slicer. The slices were approximately 3–4 μm thick, numbered, and baked at 60 °C in an oven. The following procedures were followed: HE (hematoxylin and eosin) staining, Masson's trichrome staining, EVG staining, and Sirius Red staining. HE stained sections were placed under a 200× microscope for the neutrophil count analysis, and three sections were randomly selected. Each section counted five fields, and each field counted 200 cells, and the proportion of neutrophils in these 200 cells was compared.

Statistical analysis

The data was analyzed using SPSS 21.0 statistical software (IBM Corp. Armonk, NY, USA), and the homogeneity of normal distribution and variance test were used for processing. The measurement data are expressed as the average ± standard deviation. A *t*-test was used to compare the two groups. One-way analysis of variance was used to evaluate comparisons between multiple groups. Tukey's *post-hoc* test was used to evaluate paired comparisons between groups. The chi-square test evaluated the enumerated data, which was expressed in %. All data were expressed as the mean ± SD ($*P < 0.05$, $**P < 0.01$, $***P < 0.001$).

Results and discussion

Synthesis and characterization of 3DNS

The ultrastructure observed by scanning electron microscopy is shown in Fig. 1A. The contact angle was 47°, indicating that the nanofibrous scaffolds were sufficiently hydrophilic. The nanofilaments' diameters were relatively uniform, primarily concentrated in the range of 250–300 nm, and no droplet phenomenon was observed (Fig. 1C and D). The displacement-load diagrams for RSF (regenerated silk fibrion) nanofiber scaffolds and RSF/PVA nanofiber scaffolds are depicted in Fig. 1E. The strength of nanofiber scaffolds was significantly increased after adding PVA (polyvinyl alcohol), as was fracture elongation, implying that scaffolds' elasticity was also increased after adding PVA. The infrared spectra of RSF powder, PVA particles, and two types of nanofiber scaffolds are shown in Fig. 1B. The absorption peaks of RSF powder and two types of nanofiber scaffold amide I are 1646 cm^{-1}, 1652 cm^{-1}, and 1653 cm^{-1}, respectively. The random coiling state was transformed into an α-helical structure after electrospinning. The amide II absorption peaks were 1538 cm^{-1}, 1539 cm^{-1}, and 1539 cm^{-1}, with irregular crimp structures. Between RSF/PVA and RSF nanofiber, the RSF nanofiber absorption peak position was roughly similar, only 1178 cm^{-1}, and the absorption peak size difference was high because of the C–O–C structure formed between PVA and RSF. The absorption peak position of PVA particles differed significantly from that of the RSF/PVA nanofiber scaffold, owing to RSF/PVA nanofiber scaffold's low PVA content and interaction with RSF.

We discovered that the coaxial structure was evident when the flow rate was 0.1 mL h^{-1}, with ideal drug embedding and no core–shell mutual dissolution under transmission electron microscopy (Fig. 1F and H).[25] The drug release curve was flat, and a controllable bFGF release level did not result in long-term and continuous exposure to high bFGF doses (Fig. 1G).

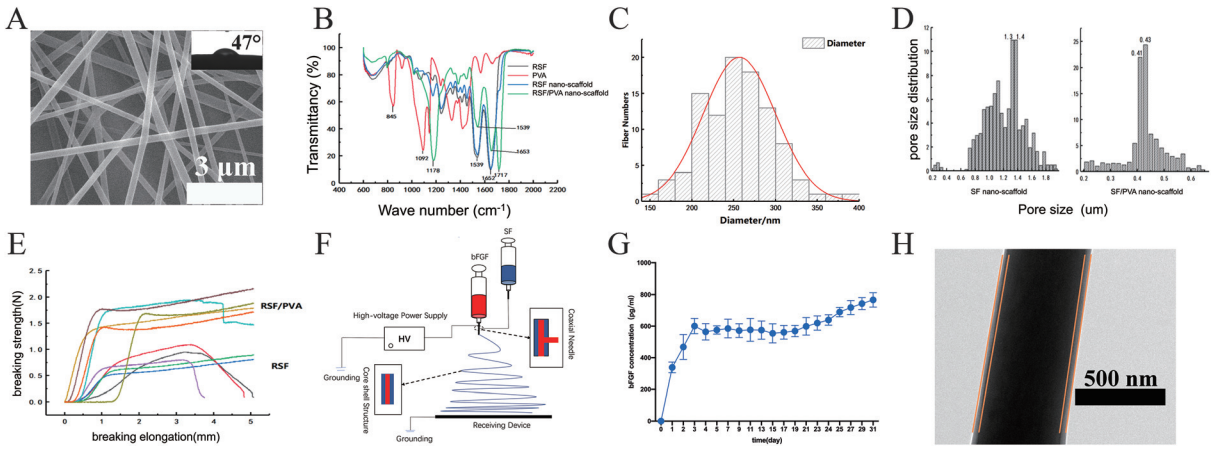

Fig. 1 The synthesis and characterization of 3DNS. (A) Representative scanning electron microscopy image showing the surface morphology of 3DNS and contact angle was 47°; (B) infrared spectra of RSF powder, PVA particles, RSF nanoscaffolds and RSF/PVA nanofiber scaffolds; (C) the diameter of the 3DNS; (D) the diameter distribution chart of the 3DNS; (E) the mechanical testing results of the SF and SF/PVA scaffolds; (F) schematic diagram of the coaxial electrospinning technology; (G) 3DNS bFGF release immersed in PBS for 31 days; (H) representative transmission electron microscopy image of 3DNS.

Transvaginal delivery and weak pelvic floor tissue are risk factors for the occurrence and development of POP, and the incidence of POP increases annually.[26] On average, one out of ten women who have vaginal deliveries needs repair surgery, and secondary surgery is as high as 13%.[27] The reason for this is that autologous repair has a high recurrence rate.

In contrast, because polypropylene mesh has a high foreign body reaction (FBR), it is a focus to develop a mesh with high histocompatibility and induce tissue regeneration. We demonstrated that bFGF could stimulate collagen regeneration[24] and thus accelerate ECM reconstruction. When combined with coaxial electrospinning,[28] overcoming a series of challenges in applying growth factors improves drug safety.[29–31] A focus would be on silk fibroin mesh combined with controlled-release technology.

Biocompatibility of 3DNS

We evaluated the cytotoxicity of ADSCs cocultured on the 3DNS. The cells of ADSCs were triangular or long spindle-shaped in the nanofiber scaffolds, which provided satisfactory attachment sites for cells; moreover, the cells fully extended and extended more synapses (Fig. 2A), suggesting that the nanofiber scaffolds had effective biocompatibility. Furthermore, as shown in Fig. 2B and C, live and dead cell staining showed that the cells on the scaffolds survived well, with no cell shedding or death. After the cells were planted on the scaffolds for the seventh day, the number of cells increased significantly, indicating that the biocompatibility of nanofiber scaffolds was efficient and suitable for cell growth. Biocompatibility is essentially a process of mutual stimulation and reaction between cells and materials. The physical properties of 3DNS, including morphology and geometry, will affect the fate of cells. The nanostructures provided by scaffolds can provide more contact sites for cells, and combined with the constantly released bFGF, the proliferation activity of cells can be improved at the initial stage.

Nanofiber scaffolds promote the differentiation of ADSCs

The groups were established as blank control, 2D-induced differentiation, and 3DNS-induced differentiation. Following 2–4 weeks of culture, western blot and analysis revealed that the 3DNS group expressed more collagen (Fig. 2D and E), and the average fluorescence intensity of FSP-1 in 3DNS group was significantly higher than in the other two groups, indicating that ADSCs differentiated into fibroblasts (Fig. 2G). The expression of the cytoskeleton and vinculin suggested that cells and biological materials interact. Immunofluorescence and cytoskeleton staining revealed that vinculin was matured in the 3DNS group. Furthermore, the cytoskeleton's fibre arrangement was orderly (Fig. 2F, H and I), which showed that the cells had good bioactivity on the scaffold.

ADSCs are clonal pluripotent stem cells that have been widely recognized for their ability to promote tissue repair[32] and have a high potential for POP therapy.[33–35] ADSCs can reduce inflammation, inhibit immune rejection, and speed up repair.[36]

However, clinical trial results revealed that stem cell injection had little therapeutic effect[37] due to a lack of extracellular matrix adhesion and failure to achieve therapeutic purposes.[38] According to research, the spatial structure of nanofibers has a significant impact on the fate of stem cells.[39] The ECM is a complex three-dimensional environment in which cells can survive and perform biological functions.[40] New bionic biomaterials can mimic the spatial specificity of the microenvironment at the implantation site, provide precise mechanical stimulation and influence stem cells. Accordingly, directional differentiation of stem cells is possible.[41,42]

Role of the integrin signaling pathway in stem cell differentiation induced by scaffolds

The microstructure of 3DNS may provide more cell contact sites, thereby promoting cell adhesion, growth, and differentiation.[42] Integrin is a heterodimer protein family that plays an essential role in mediating cell–ECM interactions and cell surface signal transduction.[43] Therefore, we examined integrin β-1 expression in three groups, and the results revealed that integrin expression increased in 3DNS group (Fig. 3A and B). Integrin may increase the amount of local adhesion due to its biological function of recognizing and binding ECM proteins. Vinculin is a focal adhesion (FA) binding protein and a component that connects integrin to the cytoskeleton,[44] but our results demonstrated that its expression was not increased (Fig. 3A and B). Fibronectin (FN), on the other hand, is an ECM glycoprotein involved in cell adhesion; integrin binds to FN in ECM, and integrin subunits amplify cascade signals and facilitate communication between cells and ECM *via* cell-surface integrin receptors for biological functions.[45] We discovered that FN expression increased in 3DNS group (Fig. 3A and B), which could provide more RGD binding sites and increase cell adhesion, influencing the downstream integrin signaling pathway. The SRC family of kinases, focal adhesion kinase (FAK), interacts with integrin bases in the cytoplasmic tail and is activated by most integrins.[46] This process promotes the phosphorylation of downstream extracellular signal-regulated kinase (ERK), which is essential for cell adhesion, growth, and differentiation.[47] Hence, we looked at the expression of FAK, P-FAK, ERK, P-ERK, COL1A1 and COL3A1 in each of the three groups. P-FAK, P-ERK, COL1A1 and COL3A1 protein expression levels were increased than in 2D group (Fig. 3A–D). Integrins have two biological functions: bind to ECM and cytoskeleton and send signals into cells.[48] Integrins communicate with cells to promote the phosphorylation of FAK and ERK, which directs the transcription of COL1 and COL3 genes.[49] This signal transduction was inhibited by FAK inhibitor, which affected collagen expression (Fig. 3E and F). Therefore, we hypothesized that ECM microenvironment created by 3DNS might regulate stem cell differentiation *via* mechanically sensitive signaling pathways mediated by integrin/FAK/ERK (Fig. 3G).

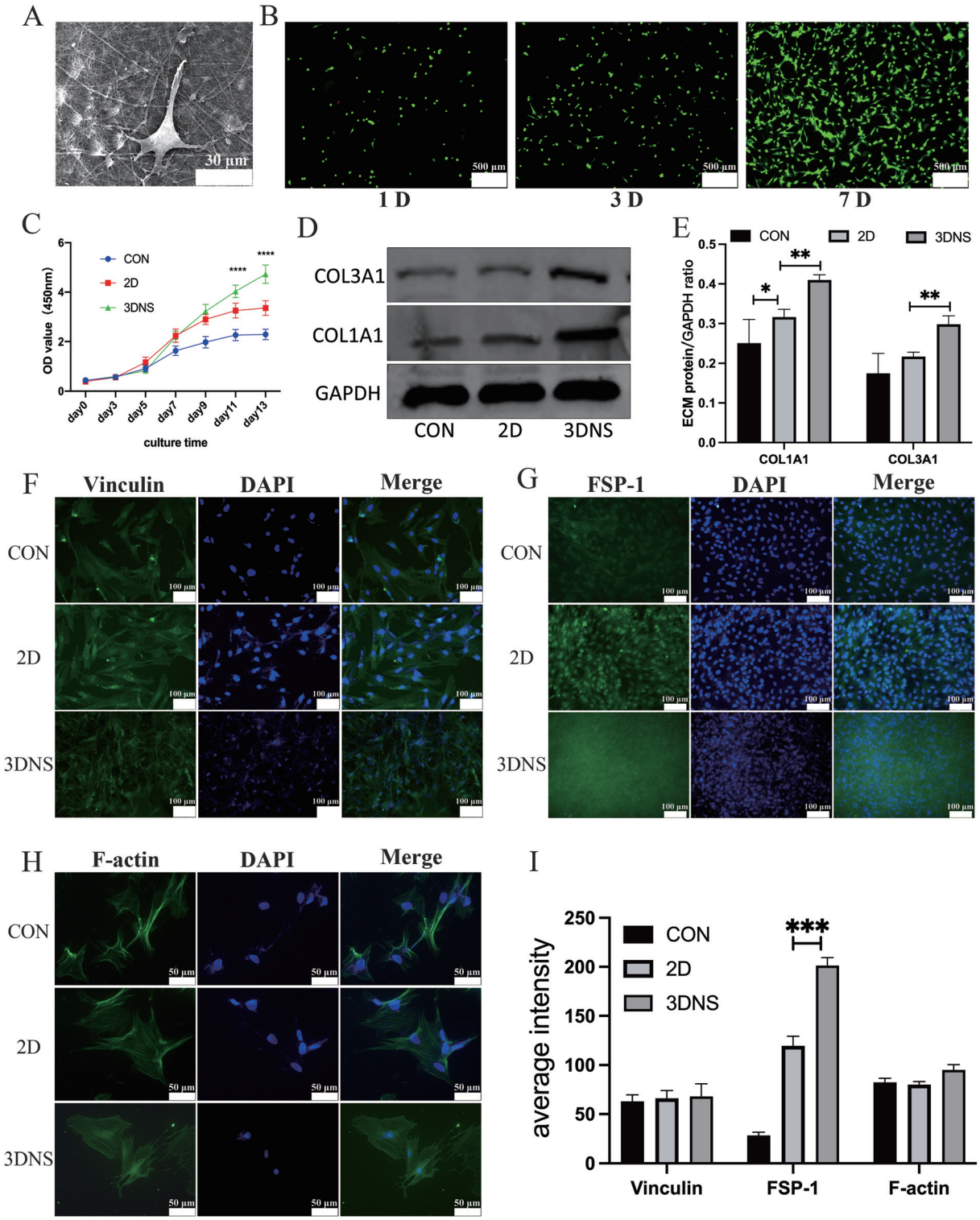

Fig. 2 The biocompatibility of 3DNS. (A) Morphology of ADSCs cultured on the 3DNS with SEM; (B) the fluorescence micrographs showed live and dead cells on 3DNS at 1, 3, and 7 days, green indicate live cells while red ones indicate dead cells; (C) viability of ADSCs of the control, 2D and 3DNS groups; (D–E) western blot analysis representative the expression of collagen proteins in the three groups; (F) representative vinculin staining images; (G) representative FSP-1 staining images; (H) representative cytoskeleton staining images; (H) corresponding quantitative intensities of vinculin, FSP-1 and cytoskeleton, *indicates significant difference at $P < 0.05$; **indicates significant difference for $P < 0.01$; ***indicates significant difference for $P < 0.001$ as compared to the control group.

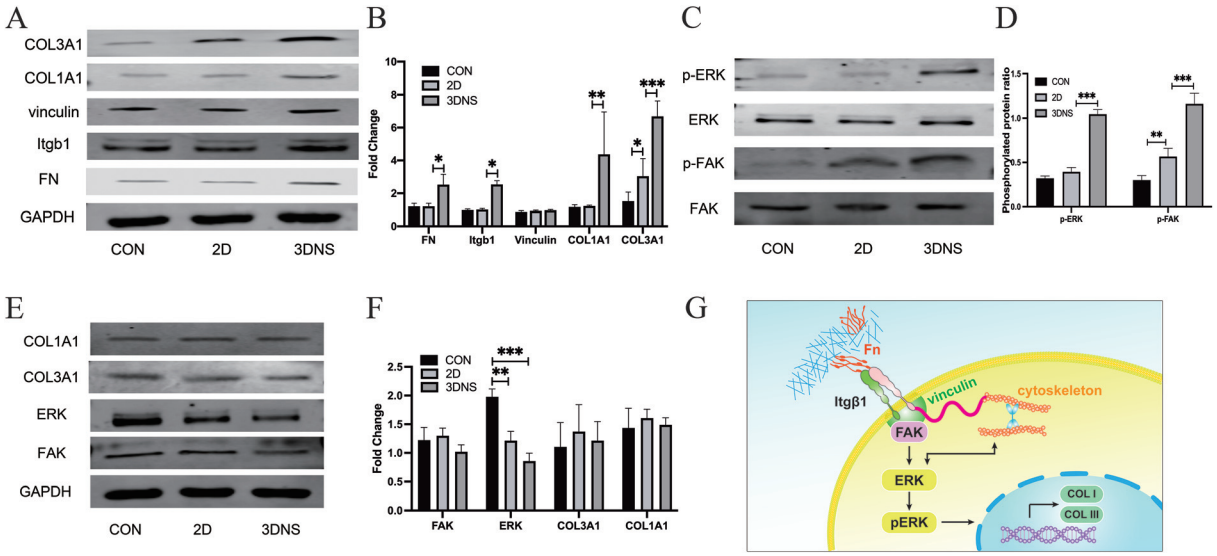

Fig. 3 3DNS promote the differentiation of ADSCs, integrin signaling pathway play a key role in stem cell differentiation induced by scaffolds. (A–D) Western blot analysis representative the expression of collagen and integrin signaling pathway related proteins in the three groups; (E and F) representative the expression after the addition of FAK inhibitor, related protein expression, *indicates significant difference at $P < 0.05$; **indicates significant difference for $P < 0.01$; ***indicates significant difference for $P < 0.001$ as compared to the control group; (G) schematic diagram of the molecular mechanism for ADSC differentiation induced by 3DNS.

The tissue engineering mesh had good histocompatibility

In vivo, there was no severe adhesion between the mesh and the subcutaneous tissue in any of the five groups, nor was there acute or chronic inflammation in the five groups (Fig. 4A). HE staining showed that the silk fibroin mesh material was dyed red, and in the pores of the mesh, cell growth and red blood cells were observed in the mesh pores, indicating the formation of new small blood vessels. Neutrophils were counted and statistically analyzed around the mesh in the early postoperative period, revealing that SF had a significantly higher early inflammatory response than the other groups (Fig. 4B and C). There were no adverse events such as subcutaneous tumours found in experimental animals, which reflects the safety of stem cells to a degree, but it is insufficiently comprehensive.

Tissue engineering mesh based on nanofiber scaffolds can promote collagen regeneration

POP models currently available include mice, rats, sheep, rabbits, primates, and pigs. Large animals, such as primates, have anatomical and organizational structures similar to humans and were thought to be the best POP model. However, there are challenges, such as a long life span, high research costs, and site constraints. Although there are anatomical differences between rodents and human beings, rodents have the advantages of easy acquisition, short life span, large quantity, and economy. Rats are small animals, with a vaginal area about 0.5 × 1.0 × 0.1 cm, a short length, and a weak vaginal wall with a mucosal fold less than that of humans, so the implantable mesh area is limited, and mechanical experiments were difficult to carry out. Furthermore, because rats are quadrupeds, the force of the pelvic floor differs from that of humans, and its pressure acts directly on the abdominal wall rather than the pelvic floor. Hence, a rat abdominal wall defect model was created. Collagen is a major component of connective tissue that supports the pelvic floor. Type I collagen primarily maintains organizational flexibility. Masson's trichrome staining revealed that collagen fibres grew around the mesh in each group, increased and arranged closely with time in all surgical groups. The collagen proportion in SF/bFGF and SF/bFGF/ADSC groups was the highest. Still, there was no significant difference between the two groups, implying that these two groups may be more advantageous in promoting extracellular matrix reconstruction (Fig. 5D and E). Sirius Red staining revealed in Fig. 5B that type I collagen was mainly produced around the mesh in SF and SF/ADSC groups in the early stage, mixed with collagen III. Tissue repair was dominated by collagen III as postoperative time was extended. Collagen III was primarily generated in SF/bFGF and SF/bFGF/ADSC groups in the early period, and a large amount of new collagen III could be observed at the 24th week after surgery, implying that these two groups of mesh materials could improve the elasticity of regenerative tissue after injury repair (Fig. 5F and G). Elastin is another essential component of ECM that helps maintain the elasticity of pelvic floor supporting tissue. Elastic fibres were stained purplish-black, and the results revealed that the control group was mainly repaired with collagen fibres, while the expression of elastic fibres in the other groups was mainly distributed around the mesh throughout the entire tissue repair period (Fig. 5C). The tensile strength of the mesh increased correspondingly at 24 weeks in SF/ADSC, SF/bFGF, and SF/bFGF/ADSC groups, but not in SF group (Fig. 5H).

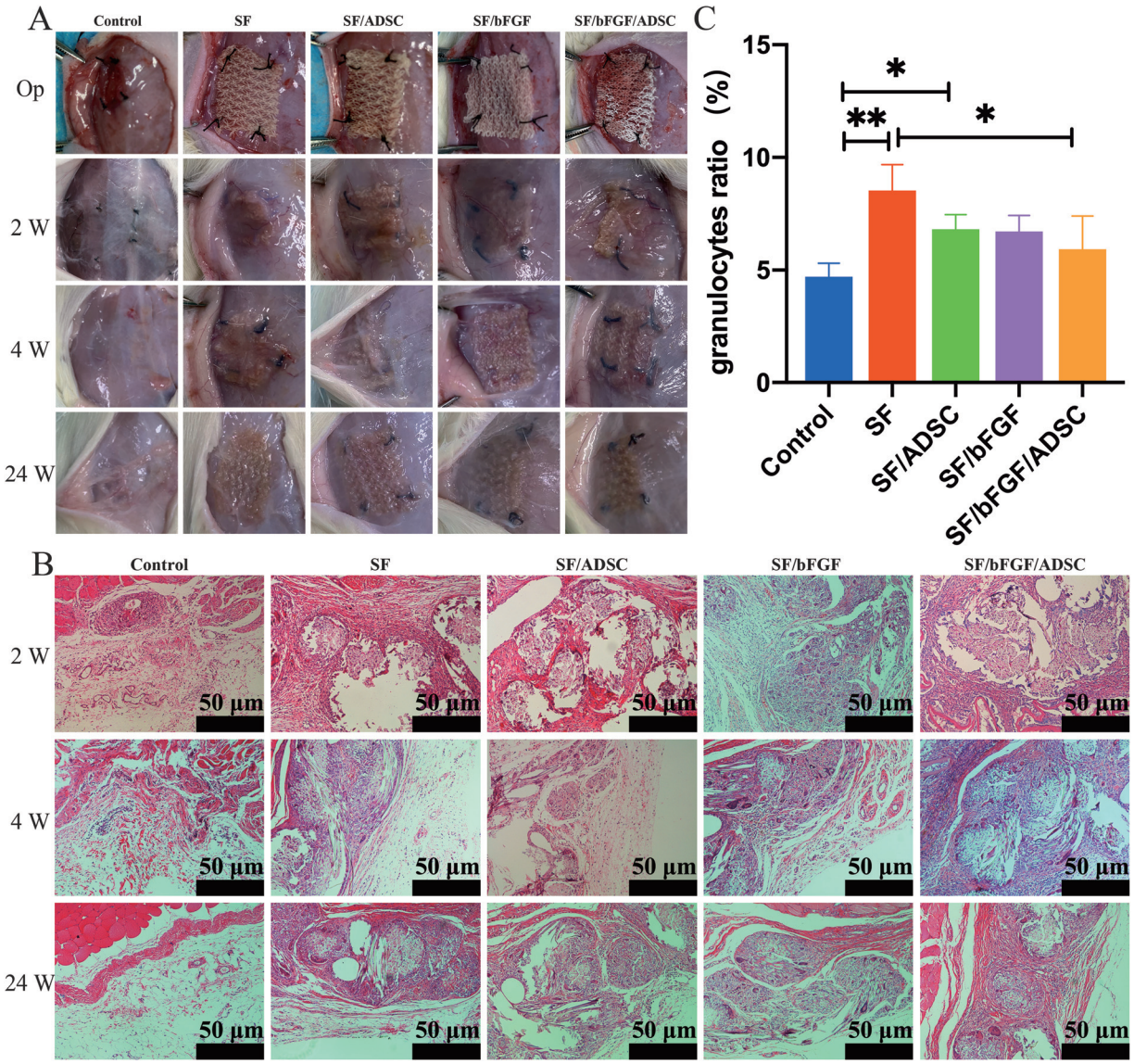

Fig. 4 The tissue engineering mesh had good histocompatibility. (A) General view of intraoperative and postoperative SD rats; (B) HE staining representing the inflammatory response around the mesh and (C) neutrophils around the mesh were counted, *indicates a significant difference at $P < 0.05$; **indicates a significant difference at $P < 0.01$; ***indicates a significant difference at $P < 0.001$ compared to the control group. The scale bar: 50 μm.

Following that, when the mechanical strength of the groups was compared, it was discovered that the mechanical strength at 24 weeks was SF/bFGF/ADSC group > SF/bFGF group = SF/ADSC group > SF group (Fig. 5I), indicating that tissue regeneration compensates for the mesh.

Tissue-engineered mesh can promote early angiogenesis

Tissue regeneration is a comprehensive and dynamic process that requires injured host cells, immune cells, cytokines and growth factors to interact, including cell migration, proliferation, angiogenesis, and fibrous tissue regeneration response,[50] in which angiogenesis is the key step for guaranteeing adequate nutrition.[51] CD31 is a vascular endothelial cell surface marker. As shown in Fig. 6A–C, the number of angiogeneses in the SF/bFGF group and SF/bFGF/ADSC group was the highest at weeks 2 and 4, and there was no difference between the two groups. At week 24, the expression of angiogenesis in the SF/bFGF/ADSC group was higher than that in the other groups. The number of blood vessels in the SF/bFGF group was significantly higher than that in the SF/ADSC group 2 weeks after surgery, and there was no difference between the two groups at 4 and 24 weeks. There was no difference in angiogenesis at each time point in the SF group, and the number of angiogeneses gradually decreased with time. Our results show that the presence of stem cells can promote angiogenesis through paracrine activity, and the presence of bFGF also synergistically promotes angiogenesis.

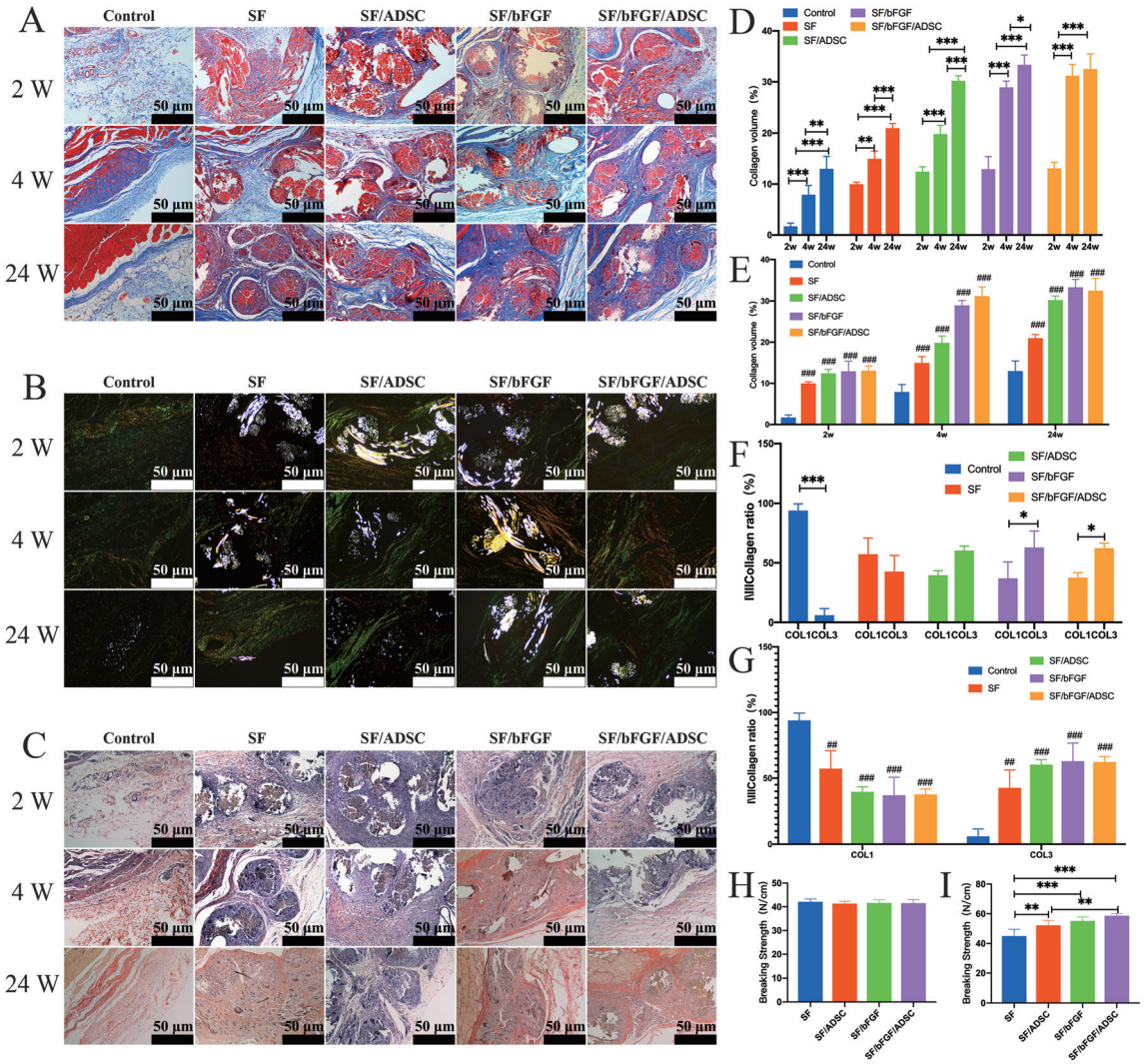

Fig. 5 Tissue engineering mesh based on nanofiber scaffolds can promote collagen regeneration. (A) Masson trichrome staining and collagen expression in each group, Masson's staining can distinguish between collagen and the muscles, the muscle fibers, red blood cells and silk fibroin mesh was dyed red, the collagen fibers was blue. The mesh were seen blue collagen fibers surrounded and blue collagen fiber grow into monofilament; (B) Sirius Red staining and the distinguish of collagen type, under polarized light represent the collagen situation around mesh in each group, type I collagen showed yellow light, type III collagen showed green light and the mesh reflected strong white light; (C) EVG staining and represented the distribution of elastic fibers, purplish black represented the elastic fibers, red represented the collagen fibers, and the background was yellow; (D) intragroup comparison of collagen volume fraction; (E) comparison of collagen volume fraction between three groups; (F and G) the proportion of type I and III collagen in each group was analysed, 5 sections were selected from each group, and 3 fields were randomly selected under polarized light, green was used as positive signal for analysis; (H and I) representative breaking stress in each group of meshes at 24 weeks. (# indicates a statistically significant difference compared with the control group, * indicates a statistically significant difference between the groups, * $P < 0.05$, ** $P < 0.01$, *** $P < 0.001$). Scale bar: 50 μm.

Tissue engineering mesh plays an important role in immune regulation

CD86 is a surface marker of M1-type macrophages, and there was no significant change in the number and generation of macrophages in different periods in the control group, more M1 were produced after mesh implantation in the other four group, which were obviously at 2 and 4 weeks after surgery and decreased to baseline level at 24 weeks and there was no significant difference in macrophage expression among all groups ((Fig. 6D–F). M1 macrophages might be produced and play a role in the early stage after mesh implantation. CD206 is a surface marker of M2-type macrophages. In Fig. 6G–I, we found that M2 production in the SF group was not significant at different stages. M2 expression was observed in the SF/ADSC group and SF/bFGF/ADSC group at the early postoperative stage and was still observed until 24 weeks after surgery. The reason may be that the stem cells in the mesh have an immunomodulatory effect and induce the transformation of M1 into M2-type macrophages. Erosion, exposure and other adverse

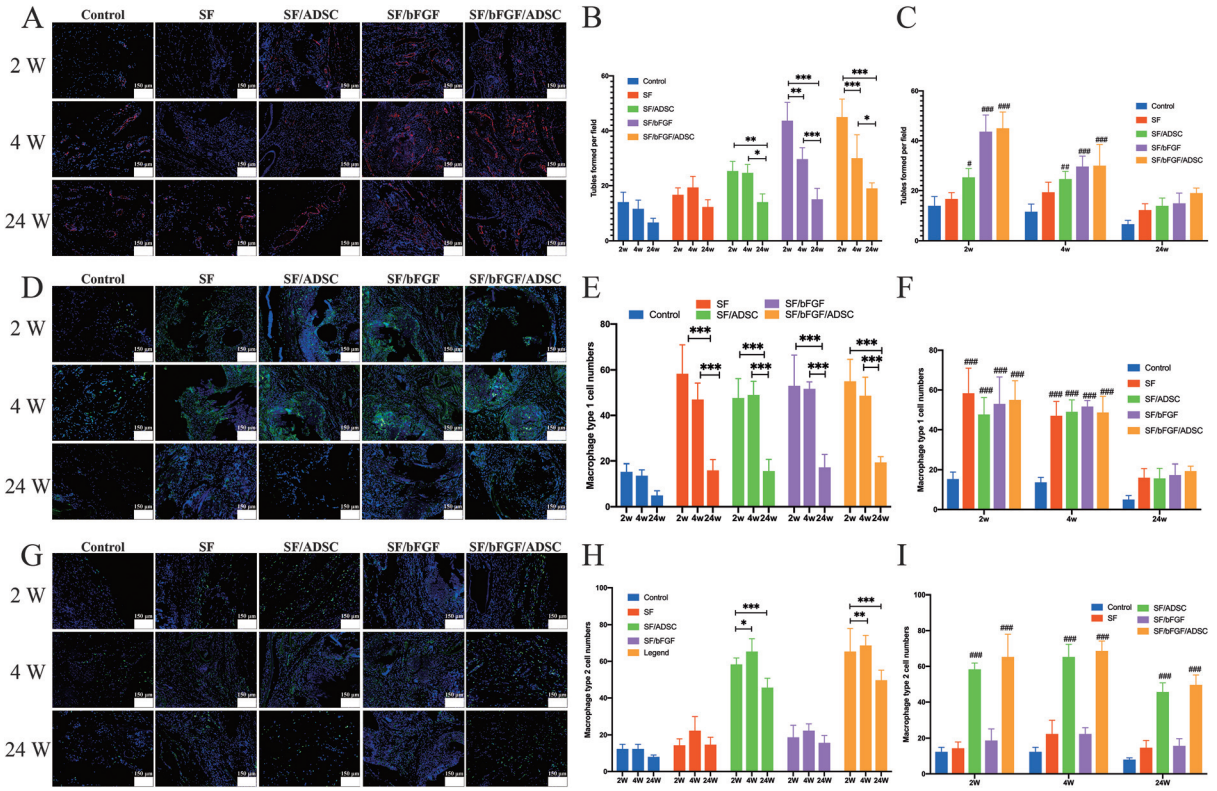

Fig. 6 The tissue engineering mesh plays an important role in promoting angiogenesis and immune regulation. (A–C) Immunofluorescence staining of CD31 for evaluating the capillary density in each group; (D–F) immunofluorescence staining of CD86 for evaluating the inflammatory response around the mesh in each group; (G–I) immunofluorescence staining of CD206 for evaluating the tissue regeneration around the mesh in each group. (# indicates a statistically significant difference compared with the control group, * indicates a statistically significant difference between the groups, * $P < 0.05$, ** $P < 0.01$, *** $P < 0.001$). Scale bar: 150 μm.

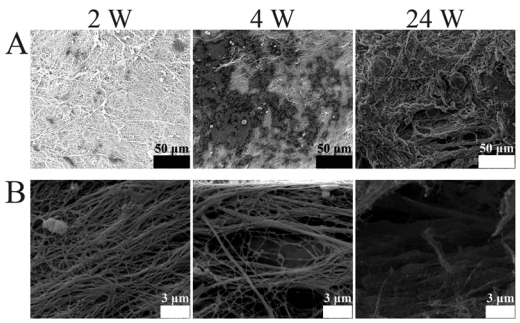

Fig. 7 Tissue engineering mesh can degrade with the prolongation of surgery. (A) Representative scanning electron microscopy image for each group; scale bar: 50 μm. (B) Enlargement of the image shown in (A). The scale bar: 3 μm.

reactions that occur in polypropylene mesh ultimately result from severe foreign body reactions, and the persistence of chronic inflammation hinders the repair process or induces mesh implantation failure,[52] in which macrophages play a leading role. Macrophages play an important role in inflammation, host defense, tissue repair and metabolism.[53] Mononuclear macrophages can differentiate into different phenotypes and play key roles in different microenvironments, which is called macrophage polarization and mutual transformation under the regulation of the surrounding tissue microenvironment.[54] The M1 reaction at the early stage of material implantation can remove dead cells and tissue debris generated surgically,[55] and the persistent presence of M1 leads to serious foreign body reaction (FBR) and granuloma formation,[56] while a higher M2/M1 ratio is conducive to tissue regeneration after biomaterial implantation. Considering that M1-type macrophages will be activated to the material surface in the early stage after material implantation, we speculated that the early transformation of M1 to M2 may be more conducive to tissue regeneration and reduce the occurrence of long-term inflammatory reactions.[57] Soluble factors secreted by ADSCs, such as IL-10, PGE2 and IL-1β are key molecules in the interaction between MSCs and macrophages and play a key role in the polarization from M1 to M2.[50] If the mesh has good biocompatibility, there would be low foreign body reaction during the tissue repair process, and collagen produced by fibroblasts can replace the missing ECM without forming scars.[58]

Tissue engineering mesh was degradable and improved the biomechanical properties of tissues

Another indicator of histocompatibility is the mesh's biodegradability. Two weeks after surgery, fibrous tissue enveloped the mesh surface, and the fibrous tissue on the mesh surface was

stripped away to reveal the nano scaffold. The scaffold fibre was flawless, with no flaws or fractures. The mesh surface was spotted, and the fibres were broken after four weeks. At 24 weeks, the scaffold structure was no longer discernible and replaced new collagen tissue (Fig. 7). The degradation rate of silk fibroin scaffolds is affected by the weaving method, the concentration of silk fibroin, and the implanted site. In our subsequent studies, the degradation time of silk fibroin scaffolds should be appropriately extended or shortened on this basis to achieve tissue regeneration and scaffold degradation rate matching.

Tissue engineering mesh have advantages compared to polypropylene mesh in the POP treatment

Materials used in tissue repair should be biocompatible to promote cell adhesion, proliferation, and differentiation while avoiding severe foreign body reactions after implantation.[59] When the mesh was implanted in the host, the surface of the mesh was quickly covered by plasma and host tissue proteins (such as immune globulin, fibronectin, and so on), attracting mononuclear cells and fibroblasts to the implanted area. The mesh surface is then covered with fibrous tissue of collagen, fibroblasts, macrophages, and foreign body giant cells.[60] If the inflammation persists, it will eventually lead to material separation from the host tissue and a slew of complications. Polypropylene mesh, both non-degradable and has poor biocompatibility, would result in a severe foreign body reaction, causing severe complications.[61] The ideal mesh should have no apparent foreign body reaction, gradually degrade and induce tissue repair, and eventually be replaced with new tissue to achieve self-repair. On the one hand, natural silk fibroin was used as the raw material of the mesh in our study, which has good biocompatibility and provided mechanical support; on the other hand, ADSCs and bFGF were added to provide a beneficial microenvironment for repair. We hope that the tissue engineering mesh attracts and regulates host cell growth, resulting in a more robust extracellular matrix to replace the mesh and repair the tissue.

Conclusions

Electrospun nanofibers have been extensively investigated as a class of scaffolding technique for tissue regeneration. We used tissue engineering approaches to POP treatment using ADSCs and new degradable nanofibrous constructs because of their unique ability to mimic the functions of ECM and drug delivery, which showed a promising therapy that may overcome the shortcomings of the polypropylene mesh through its immunomodulatory, proangiogenic, and antifibrotic effects. These findings provide potential avenues for future clinical research and help to advance the treatment of intractable POP.

Author contributions

Xiaotong Wu: investigation, writing – original draft, data curation, review and editing. Hong Guo: methodology, software, formal analysis. Yuanyuan Jia, Qing Wang and Jiaqi Wang: methodology. Jianliu Wang: project administration. Xiuli Sun: conceptualization, supervision and funding acquisition.

Conflicts of interest

There are no conflicts of interest to declare.

Acknowledgements

This work was supported by the National Natural Science Foundation of China [82171615, 82101697, 81901461, 81571420]; Peking University People's Hospital Research Development Fund [RDH2020-08]; and the National Key Technology R&D Program of China [2018YFC2002204]. We are grateful for the assistance of Figdraw.com with some pictures.

References

1 J. L. Blomquist, A. Muñoz, M. Carroll and V. Handa, *J. Am. Med. Assoc.*, 2018, **320**, 2438–2447.
2 N. Mangir, S. Roman, C. R. Chapple and S. Macneil, *World J. Urol.*, 2020, **38**, 73–80.
3 FDA and HHS, *Fed. Regist.*, 2016, **81**, 353–361.
4 A. Sedrakyan, B. Chughtai and J. Mao, *JAMA Intern. Med.*, 2016, **176**, 275–277.
5 R. Lombardo, F. C. Burkhard, A. Tubaro and European Association of Urology Urinary Incontinence Guidelines Panel Group, *Eur. Urol.*, 2019, **75**, 196–197.
6 FDA News Release, **https://www.fda.gov/news-events/press-announcements/fda-takes-action-protect-womens-health-orders-manufacturers-surgical-mesh-intended-transvaginal**, (accessed April 2019).
7 M. J. Hung, M. C. Wen, Y. T. Huang, G. D. Chen, M. M. Chou and V. C. Yang, *J. Formos. Med. Assoc.*, 2014, **113**, 704–715.
8 H. Q. Li, F. Wen, H. Z. Chen, M. Pal, Y. K. Lai, A. Z. Zhao and L. P. Tan, *ACS Appl. Mater. Interfaces*, 2016, **8**, 563–573.
9 S. E. Enderami, S. F. Ahmadi, R. N. Mansour, S. Abediankenari, H. Ranjbaran, M. Mossahebi-Mohammadi, R. Salarinia and H. Mahboudi, *Mater. Sci. Eng., C*, 2020, **108**, 110398.
10 H. Mizuno, M. Tobita and A. C. Uysal, *J. Oral Biosci.*, 2012, **30**, 804–810.
11 D. C. Ding, H. L. Chou, W. T. Hung, H. W. Liu and T. Y. Chu, *J. Biomed. Sci.*, 2013, **20**, 59.
12 M. Barba, C. Cicione, C. Bernardini, F. Michetti and W. Lattanzi, *BioMed. Res. Int.*, 2013, **2013**, 416391.
13 Z. L. Zhou, Y. H. Chen, H. Zhang, S. X. Min, B. Yu, B. He and A. Jin, *Cytotherapy*, 2013, **15**, 434–448.
14 F. Gattazzo, A. Urciuolo and P. Bonaldo, *Biochim. Biophys. Acta*, 2014, **1840**, 2506–2519.
15 S. Nadri, F. Nasehi and G. Barati, *J. Biomed. Mater. Res., Part A*, 2017, **105**, 189–197.

16 X. Y. Xie, Y. N. Wang, Y. Xia and Y. P. Mao, *Biosci. Rep.*, 2019, **39**, BSR20190433.
17 M. Motokawa, M. Kaku, Y. Matsuda, S. Kojima, C. Sumi, A. Kimura and K. Tanimoto, *Clin. Oral Investig.*, 2015, **19**, 929–935.
18 J. Yin, S. J. Qiu, B. C. Shi, X. L. Xu, Y. F. Zhao, J. H. Gao, S. L. Zhao and S. X. Min, *Biomed. Mater.*, 2018, **13**, 025001.
19 C. E. Gargett, S. Gurung, S. Darzi, J. A. Werkmeister and S. Mukherjee, *Curr. Opin. Urol.*, 2019, **29**, 450–457.
20 S. Parham, A. Z. Kharazi, H. R. Bakhsheshi-Rad, H. Ghayour, A. F. Ismail, H. Nur and F. Berto, *Materials*, 2020, **13**, 2153.
21 J. J. Xue, T. Wu, Y. Q. Dai and Y. N. Xia, *Chem. Rev.*, 2019, **119**, 5298–5415.
22 M. R. Sommer, M. Schaffner, D. Carnelli and A. R. Studart, *ACS Appl. Mater. Interfaces*, 2016, **8**, 34677–34685.
23 L. P. Yan, J. M. Oliveira, A. L. Oliveira, S. G. Caridade, J. F. Mano and R. L. Reis, *Acta Biomater.*, 2012, **8**, 289–301.
24 X. T. Wu, Y. Y. Jia, X. L. Sun and J. L. Wang, *Connect. Tissue Res.*, 2021, **19**, 1–13.
25 D. McNulty, Q. Ramasse and C. O'Dwyer, *Nanoscale*, 2016, **8**, 16266–16275.
26 K. S. Bohlin, M. Ankardal, E. Nüssler, H. Lindkvist and I. Milsom, *J. Med. Life*, 2018, **29**, 81–89.
27 M. Gyhagen, M. Bullarbo, T. F. Nielsen and I. Milsom, *BJOG Int. J. Obstet. Gynaecol.*, 2013, **120**, 152–160.
28 D. Steffens, D. I. Braghirolli, N. Maurmann and P. Pranke, *Drug Discovery Today*, 2018, **23**, 1474–1488.
29 A. Haider, S. Haider and I. K. Kang, *Arab. J. Chem.*, 2018, **11**, 1165–1188.
30 M. H. Liu, X. P. Duan, Y. M. Li, D. P. Yang and Y. Z. Long, *Mater. Sci. Eng., C*, 2017, **76**, 1413–1423.
31 Z. Abdali, S. Logsetty and S. Liu, *ACS Omega*, 2019, **4**, 4063–4070.
32 C. E. Gargett, K. E. Schwab and J. A. Deane, *Hum. Reprod. Update*, 2016, **22**, 137–163.
33 S. Darzi, J. A. Werkmeister, J. A. Deane and C. E. Gargett, *Stem Cells Transl. Med.*, 2016, **5**, 1127–1132.
34 G. Callewaert, M. Monteiro Carvalho Mori Da Cunha, N. Sindhwani, M. Sampaolesi, M. Albersen and J. Deprest, *Nat. Rev. Urol.*, 2017, **14**, 373–385.
35 C. E. Gargett, S. Gurung, S. Darzi, J. A. Werkmeister and S. Mukherjee, *Curr. Opin. Urol.*, 2019, **29**, 450–457.
36 K. L. Blanc and L. C. Davies, *Immunol. Lett.*, 2015, **168**, 140–146.
37 S. Dimmeler, S. Ding, T. A. Rando and A. Trounson, *Nat. Med.*, 2014, **20**, 814–821.
38 A. I. Hoch, V. Mittal, D. Mitra, N. Vollmer, C. A. Zikry and J. K. Leach, *Biomaterials*, 2016, **74**, 178–187.
39 J. M. Muncie and V. M. Weaver, *Curr. Top. Dev. Biol.*, 2018, **130**, 1–37.
40 O. Adamczyk, Z. Baster, M. Szczypior and Z. Rajfur, *Int. J. Mol. Sci.*, 2021, **22**, 960.
41 O. Chaudhuri, L. Gu, M. Darnell, D. Klumpers, S. A. Bencherif, J. C. Weaver, N. Huebsch and D. J. Mooney, *Nat. Commun.*, 2015, **6**, 6364.
42 J. Hao, Y. L. Zhang, D. Jing, Y. Shen, G. Tang, S. S. Huang and Z. H. Zhao, *Acta Biomater.*, 2015, **20**, 1–9.
43 J. Z. Kechagia, J. Ivaska and P. Roca-Cusachs, *Nat. Rev. Mol. Cell Biol.*, 2019, **20**, 457–473.
44 M. Bachmann, S. Kukkurainen, V. P. Hytönen and B. Wehrle-Haller, *Physiol. Rev.*, 2019, **99**, 1655–1699.
45 R. K. Das, O. F. Zouani, C. Labrugère, R. Oda and M. C. Durrieu, *ACS Nano*, 2013, **7**, 3351–3361.
46 A. Elosegui-Artola, R. Oria, Y. F. Chen, A. Kosmalska, C. Pérez-González, N. Castro, C. Zhu, X. Trepat and P. Roca-Cusachs, *Nat. Cell Biol.*, 2016, **18**, 540–548.
47 B. Lu, D. Y. Zhu, J. H. Yin, H. Xu, C. Q. Zhang, Q. F. Ke, Y. S. Gao and Y. P. Guo, *Biofabrication*, 2019, **11**, 025012.
48 D. Park, E. Wershof, S. Boeing, A. Labernadie, R. P. Jenkins, S. George, X. Trepat, P. A. Bates and E. Sahai, *Nat. Mater.*, 2019, **19**, 227–238.
49 M. J. Dalby, N. Gadegaard and R. O. C. Oreffo, *Nat. Mater.*, 2014, **13**, 558–569.
50 A. Cristina de Oliveira Gonzalez, T. Fortuna Costa, Z. Araújo Andrade and A. Ribeiro Alves Peixoto Medrado, *An. Bras. Dermatol.*, 2016, **91**, 614–620.
51 S. A. Eming, B. Brachvogel, T. Odorisio and M. Koch, *Prog. Histochem. Cytochem.*, 2007, **42**, 115–170.
52 A. Przekora, *Mater. Sci. Eng., C*, 2019, **97**, 1036–1051.
53 S. Vieira, A. S. Morais, E. Garet, J. Silva-Correia, R. L. Reis, Á. González-Fernández and J. M. Oliveira, *Acta Biomater.*, 2019, **93**, 74–85.
54 M. Barbeck, L. Kühnel, F. Witte, J. Pissarek, C. Precht, X. Xiong, R. Krastev, N. Wegner, F. Walther and O. Jung, *J. Mol. Sci.*, 2020, **28**, 3098.
55 M. L. Novak, E. M. Weinheimer-Haus and T. J. Koh, *J. Pathol.*, 2014, **232**, 344–355.
56 S. Franz, S. Rammelt, D. Scharnweber and J. C. Simon, *Biomaterials*, 2011, **32**, 6692–6709.
57 R. Klopfleisch and F. Jung, *J. Biomed. Mater. Res., Part A*, 2017, **105**, 927–940.
58 M. L. Xue and C. J. Jackson, *Adv. Wound Care*, 2015, **4**, 119–136.
59 A. Przekora, *Mater. Sci. Eng., C*, 2019, **97**, 1036–1051.
60 G. Tullii, F. Giona, F. Lodola, S. Bonfadini, C. Bossio, S. Varo, A. Desii, L. Criante, C. Sala, M. Pasini, C. Verpelli, F. Galeotti and M. R. Antognazza, *ACS Appl. Mater. Interfaces*, 2019, **11**, 28125–28137.
61 Y. J. Xie, C. Hu, Y. Feng, D. F. Li, T. T. Ai, Y. L. Huang, X. D. Chen, L. J. Huang and J. L. Tan, *Regen. Biomater.*, 2020, **7**, 233–245.